

Differentiable Microscopy Designs an All Optical Quantitative Phase Microscope

Kithmini Herath^{2,†}, Udith Haputhanthri^{1,2,†}, Ramith Hettiarachchi^{2,†}, Hasindu Kariyawasam^{2,†}
Azeem Ahmad³, Balpreet S. Ahluwalia³, Chamira U. S. Edussooriya², and Dushan N. Wadduwage^{1,*}

¹Center for Advanced Imaging, Faculty of Arts and Sciences, Harvard University, Cambridge, USA

²Department of Electronic and Telecommunication Engineering, University of Moratuwa, Sri Lanka

³UiT The Arctic University of Norway

*wadduwage@fas.harvard.edu

Abstract

Ever since the first microscope by Zacharias Janssen in the late 16th century, scientists have been inventing new types of microscopes for various tasks. Inventing a novel architecture demands years, if not decades, worth of scientific experience and creativity. In this work, we introduce Differentiable Microscopy ($\partial\mu$), a deep learning-based design paradigm, to aid scientists design new interpretable microscope architectures. Differentiable microscopy first models a common physics-based optical system however with trainable optical elements at key locations on the optical path. Using pre-acquired data, we then train the model end-to-end for a task of interest. The learnt design proposal can then be simplified by interpreting the learnt optical elements. As a first demonstration, based on the optical 4-f system, we present an all-optical quantitative phase microscope (QPM) design that requires no computational post-reconstruction. A follow-up literature survey suggested that the learnt architecture is similar to the generalized phase concept developed two decades ago. We then incorporate the generalized phase contrast concept to simplify the learning procedure. Furthermore, we also demonstrate that similar results can be achieved by an uninterpretable learning based method, namely diffractive deep neural networks (D2NN). We outperform the existing benchmark for all-optical phase-to-intensity conversion on multiple datasets, and ours is the first demonstration of its kind on D2NNs. The proposed differentiable microscopy framework supplements the creative process of designing new optical systems and would perhaps lead to unconventional but better optical designs.

1. Introduction

Even though the invention of microscopes dates back to the late 16th century, it was during the late 19th to 20th century that the field saw a major renaissance [1]. This is especially due to the requirement of cross-domain scientific knowledge and creativity. For instance, as much as the knowledge of physics that is essential to build optical systems, fields such as chemistry (for sample preparation) and computer science (for image post-processing), play an important role in developing novel microscope architectures. Typical microscopy instrumentation involves understanding: the light-matter interaction at the specimen, how light propagate through optics, and how the final image is formed. The scientist’s job is to design the optics such that the final image contains desired information about the measurands. This creative process may require enormous fuzzy calculations on the light propagation just to initialize a potential optical design. In this work, we explore how machine learning can help ignite the creative design process for a new measurement task in a top-down approach.

Deep learning has been increasingly used in various microscopy methods to perform tasks such as denoising, image reconstruction, and classification [2–4]. Despite the significant performance boost in such methods, the limitations inherited from the hardware of the microscope set the upper performance bound [5]. Therefore, over the past decade, researchers have focused on joint deep-learning optimization of not only the reconstruction model but also the hardware of the microscope itself [6–11]. Nevertheless, all these methods’ focus was to optimize a system that is already capable of a specific imaging task. In contrast, we focus on the *use of machine learning to discover new optical systems* to do a new task; in other words, here our main focus is on the optical design process itself, rather than data-driven optimization of an *existing design*. To

[†] These authors contributed equally to the work.

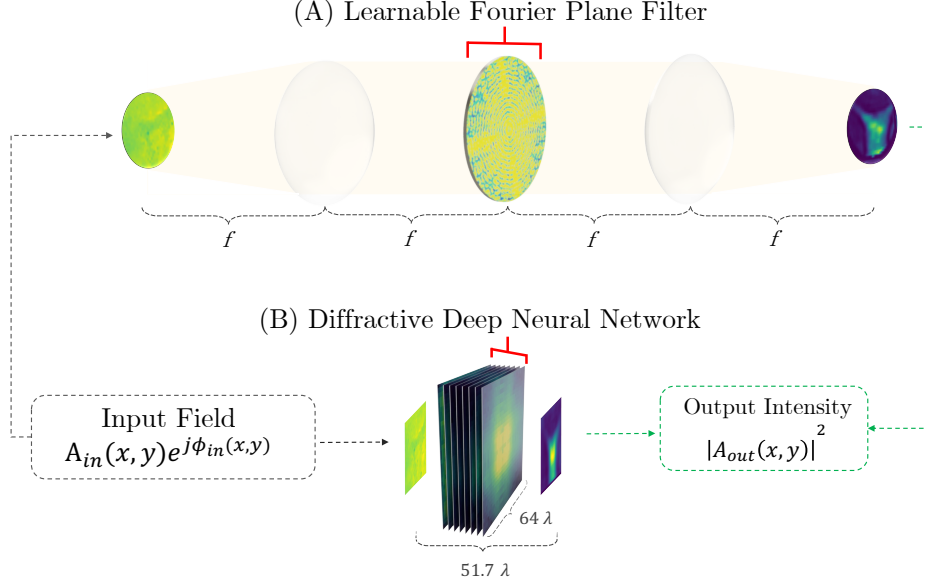


Figure 1. **Differentiable microscopy ($\partial\mu$) based all-optical phase to intensity conversion.** (A) Learnable Fourier filter (LFF) based design. Here, f denotes the focal length of the lens used to implement the 4- f system. (B) Diffractive deep neural network based design (PhaseD2NN). Here λ is the operating wavelength. Note that PhaseD2NN is very compact and less than $50\mu m$ (i.e. 51.7λ) thick.

this end, we propose differentiable microscopy ($\partial\mu$), a deep learning-based design paradigm, to design new interpretable microscope architectures without requiring considerable domain knowledge.

We chose all-optical quantitative phase measurement as a first problem for $\partial\mu$. Measuring phase information of a light field is a longstanding problem in optics with valuable applications in live cell imaging [12–16]. Live cells are thin and transparent. They are referred to as phase objects as they mainly affect the phase of the light field. Imaging devices however only measure the intensity of light. To measure the phase, sophisticated interferometric systems are needed. This class of instruments are called quantitative phase microscopes (QPMs). QPMs interfere the phase object’s light wave (object wave) with a second known light wave (called the reference wave) resulting interference patterns (called interferograms). Phase images are then reconstructed from interferograms, by computationally solving an inverse problem (we include a comprehensive discussion of more related work in the supplementary section A for the interested reader). In this work, we use differentiable microscopy to design a quantitative phase microscope (QPM) that does not require computational reconstruction. In our design the resulting interference pattern (i.e. the intensity variation at the detector) itself is the phase image (i.e. the phase variation of the object wave).

All-optical phase to intensity conversion is a challenging design task with no general analytical solution using linear optics. Thus we first formulated the problem as a learning task (section 2.1). Second, we confirmed the existence of approximate solutions for given data distributions by training a complex linear convolutional neural network (CNN) mimicking optical constraints (section 2.2). Third, for the same task, we trained a simple $\partial\mu$ architecture based on the optical 4- f system and a Fourier filter (section 2.3). The selection of the architecture was driven by the fact that a lense can optically perform Fourier Transform, and hence convolutions as multiplications. No explicit knowledge about interferometry was used during the design of the architecture. Interestingly, in a followup literature survey we found a similar design called the generalized phase contrast (GPC) method introduced by Glückstad, through careful analytical treatment of the problem [17]. We interpreted our learned $\partial\mu$ design in comparison to GPC, and performed an analysis by starting the optimization procedure from the generalized phase contrast filter. Next, for the same task, we trained a diffractive deep neural network (D2NN) [18], as an uninterpretable optical design (section 2.4). D2NN design compacts the system at the cost of interpretability. We extensively compared the performance of competing designs on simulated and experimental datasets. Our results show that the learned all-optical designs provide better reconstruction quality than the conventional GPC method. More importantly, our results suggest that given data, $\partial\mu$ can design new interpretable optical systems in a top-down fashion.

2. Results

2.1. All-optical Phase to Intensity Conversion as a Learning Problem

In a machine learning perspective, all-optical phase to intensity conversion is an image translation task. A computer model, subject to the physics of light propagation (*the rules*), should learn to translate complex-valued optical fields (inputs), to intensity maps proportional to the input phase (outputs). This task should be embedded in a loss function (*the questions*) and training data (*the correct answers*).

To this end, we first introduce **phase reconstruction loss**, \mathcal{L}_ϕ . An input optical field, $x_{in} = A_{in}e^{j\phi_{in}}$ is propagated through the proposed model H to produce the output field $x_{out} = A_{out}e^{j\phi_{out}} = H(x_{in})$. Then phase reconstruction loss is defined as,

$$\mathcal{L}_\phi = \mathbb{E}_{x_{in} \sim P_X} [Rh(|A_{out}|^2, \phi_{in}/(2\pi))], \quad (1)$$

where, P_X , and $Rh(\cdot)$ respectively represent the probability distribution of phase objects and the below-defined Reverse Huber Loss [19].

$$Rh_\delta(y, f(x)) = \begin{cases} |y - f(x)| & \text{for } |y - f(x)| \leq \delta \\ \frac{(y - f(x))^2 + \delta^2}{2\delta} & \text{otherwise.} \end{cases} \quad (2)$$

We chose the Reverse Huber Loss over L1 or MSE loss as it produces better reconstruction quality (based on the empirical results). We set the δ threshold to 0.95 of the standard deviation of the ground truth image following a similar procedure to [20]. In \mathcal{L}_ϕ however, the constant of proportionality of the objective (i.e. of $|A_{out}|^2 \propto \phi_{in}$) is fixed. We propose a second **Learned Transformation Loss**, \mathcal{L}_{LT} , which relaxes the model to learn a constant of proportionality (S).

$$\mathcal{L}_{LT} = \mathbb{E}_{x_{in} \sim P_X} \left[Rh \left(\frac{|A_{out}|^2}{S}, \frac{\phi_{in}}{2\pi} \right) \right], \quad (3)$$

\mathcal{L}_{LT} is more consistent with the problem formulation in the literature [17].

In our formulation, the input to the model is a complex-valued optical field and the output is proportional to phase of the input. Thus, we only require input optical fields as training data. We either simulated these optical fields or experimentally measured them from phase objects. We considered three simulated data sets, (1) Phase MNIST data set, (2) Phase FashionMNIST data set (3) Phase Noise data set; and two experimental datasets (4) HeLa Cell data set, (5) Bacteria data set. Details of the data sets are presented in the materials and methods section 5.1. Using the above loss functions and training data, we trained three models to convert phase to intensity: (1) A complex-valued linear convolutional neural network (CNN) mimicking optical constraints; (2) $\partial\mu$ architecture based on the optical 4- f system and a Fourier filter; (3) A PhaseD2NN. In the next sections we discuss these models and their results.

2.2. Complex-valued Linear CNN: Feasibility of Linear Phase Retrieval

All optical phase to intensity conversion is analytically unsolvable for an arbitrary input. We, therefore, first established the existence of approximate solutions to our data distributions. To do that, we trained a complex-valued linear CNN imitating optical constraints. The CNN consisted of five convolutional layers. Each layer contained a single-channel complex-valued kernel [21] of size three and no non-linear activations. Adding a bias term at each layer violates optical constraints. But adding a single bias term at the output is analogous to adding a reference arm in an optical model. Thus a bias term was added only to the last layer. The final model of the CNN is shown in the Fig. 2-A.

Table 1 and Fig. 2B-E show the results of the complex-valued CNN. As seen, the model achieved SSIM values above 0.9 for all data sets except for the HeLa $[0, 2\pi]$. The SSIM for HeLa $[0, 2\pi]$ was around 0.7. Qualitative results agree with this observation (see Fig. 2D3). Thus our complex-valued CNN, established the existence of linear approximate solutions for given data distributions, while also setting empirical upper bounds for the task on each data set.

2.3. Learnable Fourier Filter: Interpretable All-optical Phase Retrieval

Our complex-valued CNN suggests that all-optical phase to intensity conversion is possible through linear convolutions. In the second model we optically implemented these convolutions. Fig. 3A shows the optical schematic of the model. The model consisted of an optical 4- f system (see supplementary section B.1.1) and a circular Fourier filter. The filter was on a 128×128 grid of transmission coefficients. The coefficients inside the filter were treated trainable; the ones outside were set to zero (see filters in Fig. 3). The input/output of the model was of the same size as the filter. But the information of the phase

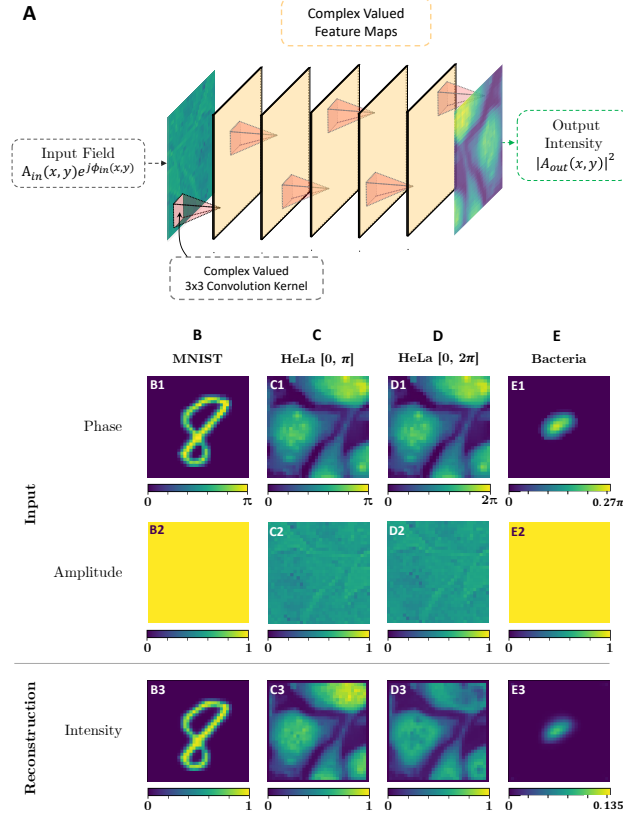


Figure 2. **Feasibility of linear phase retrieval using a complex-valued linear CNN.** (A) The network architecture. Note that there are no non-linear activations between convolutions. (B-E) Representative phase to intensity conversion results on MNIST, HeLa $[0, \pi]$, HeLa $[0, 2\pi]$, and Bacteria test data sets. The output intensity maps are visually similar to the input phase maps, suggesting a linear model can learn to convert phase to intensity for a given data set.

Dataset	Performance	
	SSIM \uparrow	L1 \downarrow
Phase MNIST $[0, \pi]$ (\mathcal{L}_ϕ)	0.9727	0.0125
Phase MNIST $[0, \pi]$ (\mathcal{L}_{LT})	0.9723	0.0138
HeLa $[0, \pi]$ (\mathcal{L}_ϕ)	0.9052	0.0302
HeLa $[0, \pi]$ (\mathcal{L}_{LT})	0.9046	0.0319
HeLa $[0, 2\pi]$ (\mathcal{L}_ϕ)	0.7059	0.0635
HeLa $[0, 2\pi]$ (\mathcal{L}_{LT})	0.6818	0.0677
Bacteria $[0, 2\pi]$ (\mathcal{L}_ϕ)	0.9631	0.0019
Bacteria $[0, 2\pi]$ (\mathcal{L}_{LT})	0.9660	0.0019

Table 1. **Performance of complex-valued linear CNNs.** The structural similarity index measure (SSIM) and the L1 distance, between the ground-truth phase and the output intensity are shown for each test data set.

object was placed within the small circular aperture on a 32×32 grid. The grid was padded $4\times$ to make up the 128×128 input to maintain a sufficient frequency sampling according to the Nyquist criterion. The first lens of the $4-f$ system, Fourier-transforms the input field; the filter linear-transforms the field; and the second lens, inverse-Fourier-transforms the field back to the spatial domain. This physical system can be mathematically modeled as in the eq. (4)

$$H\{\cdot\} \equiv IDFT2\{H_t \circ DFT2\{\cdot\}\} \quad (4)$$

where H_t represents the learnable transmission coefficient matrix. The coefficients of the filter were initialized either randomly or based on GPC-initialization (see supplementary section B.1.2) and optimized on each training data set, through the loss functions in eq. (1) and eq. (3). We conducted a series of ablation experiments to evaluate and improve the performance of the learnable Fourier filter on each dataset. We started with randomly initializing the weights of the learnable Fourier filter. Then, to investigate the optimality (or the lack of) of GPC, we initialized LFF weights from the GPC filter (LFF + GPC init) and further trained the LFF. Finally, to introduce an additional flexibility to the learning process we utilized the \mathcal{L}_{LT} for the GPC initialized model. We discuss the results of these experiments on each data set below.

Performance on Phase MNIST Digit Dataset. Table 2 shows our ablation study for the proposed learnable Fourier filter (LFF) on Phase MNIST digit dataset. LFF outperformed the GPC method by a large SSIM margin of 0.38. GPC-based initialization was comparable to random initialization but \mathcal{L}_{LT} loss slightly improved the SSIM (by 0.03) compared to \mathcal{L}_ϕ loss. Qualitative results of the study are shown in Fig. 3-B1-6. The GPC method (Fig. 3-B3) failed to generate complete dark background. In contrast, LFF reconstructed the background and foreground appropriately (Fig. 3-B4,5,6). We also experimented on the generalizability of the LFF learned from MNIST data, on the unseen FashionMNIST dataset. The resulting SSIM was 0.4665, suggesting weak generalizability (qualitative results depicted in Fig. 4). This result agrees with our further generalizability tests (see supplementary section C.2).

Performance on the HeLa Dataset. Table 2 shows the ablation study of the proposed method on HeLa datasets. The LFF outperformed the GPC method with 0.1863 SSIM margin on HeLa $[0, 2\pi]$ dataset (also see supplementary section 5.1). On HeLa $[0, \pi]$ dataset the SSIM improved by 0.119. GPC-based initialization showed no notable improvement. Interestingly, \mathcal{L}_{LT} degraded the performance in terms of SSIM on HeLa $[0, 2\pi]$, but improved in terms of L1 distance. This may be due to the optimal convergence point of our objective function (eq. 3) being similar to the optimal convergence point of the L1 distance. The qualitative results for the $[0, \pi]$ version (Fig. 3-C4,5,6) demonstrates a clearly improved contrast between the background and foreground of the cell images compared to the results of the $[0, 2\pi]$ version (Fig. 3-D4,5,6).

Performance on the Bacteria Dataset. The performance of the learnable Fourier filter on the Bacteria dataset is demonstrated in Table 2. LFF’s SSIMs were better than that of the GPC method by a large margin. Neither GPC-based initialization, nor \mathcal{L}_{LT} loss further improved results. The qualitative results of the study are shown in Fig. 3-E1-6, which depicts how the LFF in all instances has almost completely captured the exact structural content of the Bacteria compared to the ground truth phase content. Considering the quantitative results in Table 2 and qualitative results in Fig. 3-E3, the GPC method failed in reconstructing the phase content specially in the dark background regions.

2.4. Phase D2NN: Uninterpretable All-optical Phase Retrieval

Our third model is a *Diffractional Deep Neural Network*, we call *PhaseD2NN* (see supplementary section A for a brief review of D2NNs). The model consists of a large number of parameters distributed in partially-connected cascade of diffractive layers. A stand-alone layer is functionally similar to the learnable filter in the previous section. But their placement and combined function cannot be interpreted to draw insights on optical design. Nevertheless PhaseD2NN is an interesting miniaturized design, and to the best of our knowledge, this is the first demonstration of phase-to-intensity conversion using D2NNs (see supplementary section B.2 for details on mathematical modeling of D2NNs).

The proposed architecture is shown in Fig. 5A. The network consisted of 8 diffractive layers which were separated by 5.3λ distance (λ is the operating wavelength of the input field). Each layer of the network consisted of a 128×128 neuron grid that contained trainable complex-valued transmission coefficients. The size of each neuron was $\lambda/2 \times \lambda/2$. The input to the network was a light field, i.e. a complex-valued image, where the information of interest can be found in its phase. This input was located in a 32×32 grid, 5.3λ before the first layer of the D2NN. The reconstruction plane (i.e. the image plane where a detector is placed) was at a 9.3λ distance from the last optical layer. The reconstruction was done on 32×32 grid on this reconstruction plane. The element size of the input grid and reconstruction grid was same as the size of a neuron. Hence, this compact system has dimensions of $64\lambda \times 64\lambda \times 51.7\lambda$.

After mathematically modelling the diffractive layers as mentioned in supplementary section B.2, the learnable transmission coefficients (t_i) of each layer were optimized with the objective defined in eq. (1) and eq. (3). To maintain the passive nature of the layers, we constrained the amplitudes of the transmission coefficients to the range $[0, 1]$. PhaseD2NNs’ results are discussed below.

Performance on Phase MNIST Digit Dataset. Table 2 and Fig. 5B show the evaluation performances of PhaseD2NN on the Phase MNIST digit dataset. The PhaseD2NN’s SSIM was 0.9146, a significant improvement of 0.40 compared to the

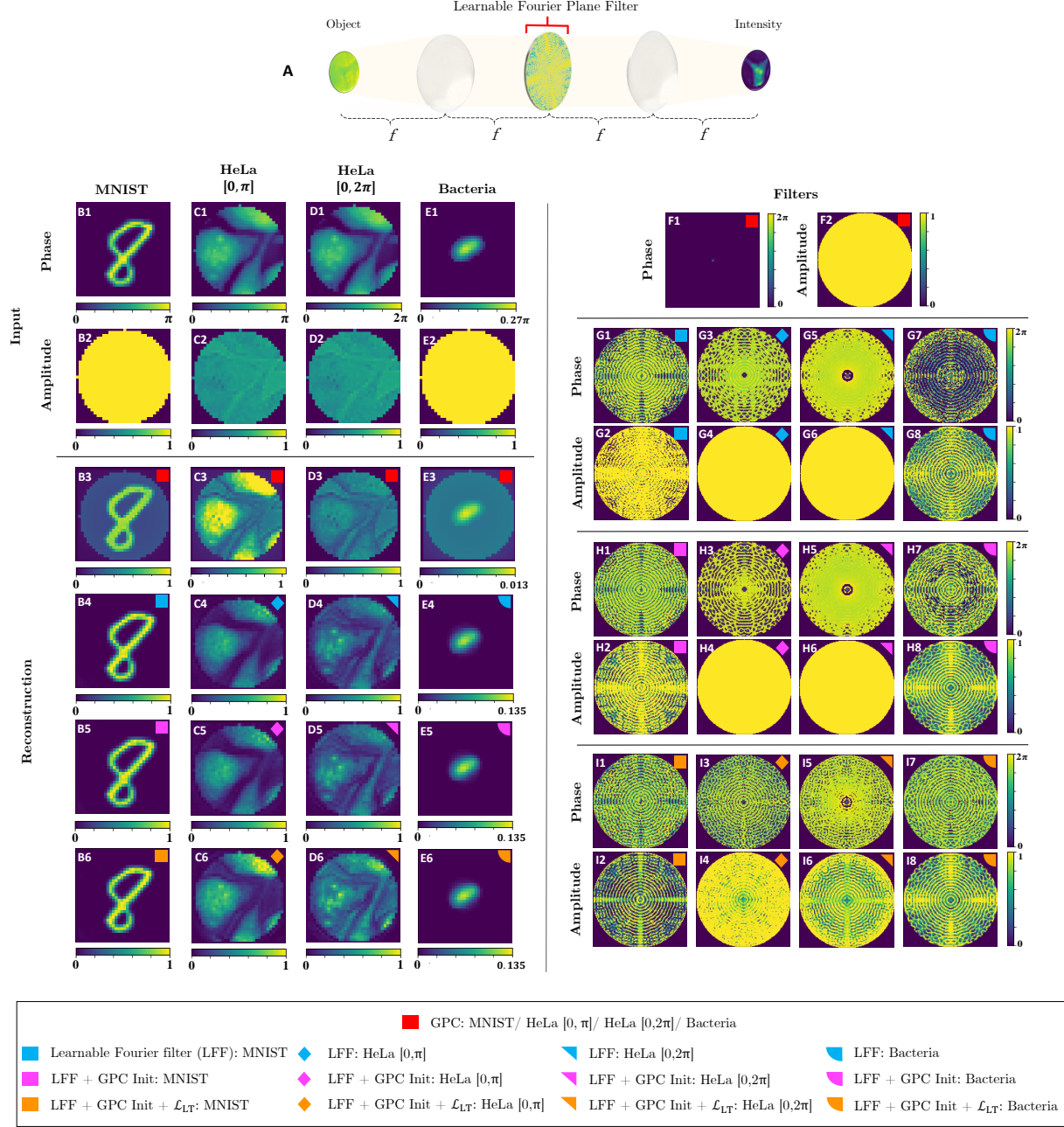


Figure 3. **Learnable Fourier filter (LFF) for all-optical phase to intensity conversion.** (A) The optical design. LFF is placed at the Fourier plane of a 4- f system. The system converts phase maps at the input image plane to intensity maps at the output image plane. (B1-6) The input phase map (B1), the input amplitude map (B2), and the reconstructed intensity maps (B3-6) for a representative test image from the Phase MNIST data set. 'B3' shows the reconstruction from the generalized phase contrast (GPC) method. 'B4-6' show the reconstructions from the proposed LFF (refer to the legend for experimental settings). (C1-6) Similar results as in 'B' for the HeLa $[0, \pi]$ test data set. (D1-6) Similar results as in 'B' for the HeLa $[0, 2\pi]$ test data set. (E1-6) Similar results as in 'B' for the bacteria test data set. (F1-18) The corresponding learned filters for each reconstruction (refer to the legend). These qualitative results show that LFF outperforms the GPC method on all data sets by learning a specialized Fourier filter for each data set.

Method	Loss		Performance	
	\mathcal{L}_ϕ	\mathcal{L}_{LT}	SSIM \uparrow	L1 \downarrow
Generalized Phase Contrast (GPC)				
MNIST: GPC*	–	–	0.5134	0.1853
HeLa $[0, \pi]$: GPC*	–	–	0.5652	0.1726
HeLa $[0, 2\pi]$: GPC*	–	–	0.4056	0.1270
Bacteria $[0, 2\pi]$: GPC*	–	–	0.6740	0.0092
Learnable Fourier Filter (LFF)				
MNIST: LFF	✓	✗	0.8933	0.0267
+ GPC init	✓	✗	0.8991	0.0269
+ GPC init	✗	✓	0.9184	0.0228
Generalizability on FashionMNIST			0.4665	0.2330
HeLa $[0, \pi]$: LFF	✓	✗	0.6842	0.1025
+ GPC init	✓	✗	0.6846	0.1026
+ GPC init	✗	✓	0.7217	0.0843
HeLa $[0, 2\pi]$: LFF	✓	✗	0.5919	0.1133
+ GPC init	✓	✗	0.5921	0.1133
+ GPC init	✗	✓	0.5719	0.1050
Bacteria $[0, 2\pi]$: LFF	✓	✗	0.9818	0.0009
+ GPC init	✓	✗	0.9816	0.0009
+ GPC init	✗	✓	0.9820	0.0010
PhaseD2NN				
MNIST:	✓	✗	0.8072	0.0402
MNIST:	✗	✓	0.9146	0.0253
Generalizability on FashionMNIST			0.5492	0.1148
HeLa $[0, \pi]$:	✓	✗	0.4386	0.1367
HeLa $[0, \pi]$:	✗	✓	0.6254	0.1059
HeLa $[0, 2\pi]$:	✓	✗	0.4854	0.1417
HeLa $[0, 2\pi]$:	✗	✓	0.4654	0.1237
Bacteria $[0, 2\pi]$:	✓	✗	0.9891	0.0008
Bacteria $[0, 2\pi]$:	✗	✓	0.9915	0.0007

* Output is scaled for each dataset (see supplementary section B.1.3)

Table 2. **Overall quantitative results.** Performance of the GPC method, the learnable Fourier filter (LFF), and the PhaseD2NN are shown for each data set at different experimental methods. The colored SSIM values depict the maximum achievable SSIM values for each dataset by the LFF and the PhaseD2NN. Same values are compared side-by-side in Fig. 6.

GPC method. The SSIM slightly improved with \mathcal{L}_{LT} . For both \mathcal{L}_ϕ and \mathcal{L}_{LT} losses, SSIMs were comparable (but slightly lower) to that of LFF. The PhaseD2NN trained on MNIST dataset still achieves an SSIM score of 0.5492 for the unseen FashionMNIST dataset. This was a notable 0.0827 increase from LFF’s generalizability SSIM (also see Fig. 4 for qualitative results). Thus compared to LFF, PhaseD2NN might better generalize across datasets with similar complexity.

Performance on the HeLa Dataset. Table 2 shows the performance of PhaseD2NN on two variants of the HeLa cell dataset. The model performed better on HeLa $[0, \pi]$ dataset than on HeLa $[0, 2\pi]$. Interestingly, when trained with \mathcal{L}_ϕ on HeLa $[0, \pi]$

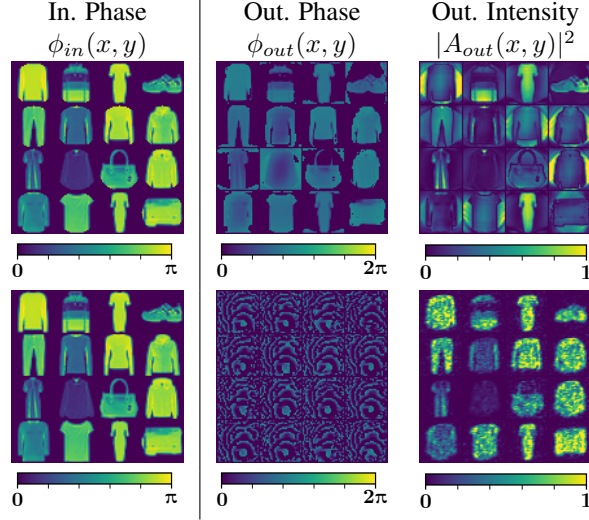


Figure 4. **Generalizability results.** The learnable Fourier filter (first row) and PhaseD2NN (second row) were trained on the MNIST dataset and were evaluated on FashionMNIST dataset. PhaseD2NN seems to generalize better than the learnable Fourier filter.

the SSIM was lower than that of GPC by a considerable 0.13 amount. But the SSIM significantly improved, beyond the GPC-level, with \mathcal{L}_{LT} loss. With both losses PhaseD2NN performed significantly worse than LFF. On HeLa $[0, 2\pi]$ dataset, PhaseD2NN beat GPC, but performed much weaker compared to LFF (0.1 SSIM margin). Qualitative results agree with these observations and are shown in Fig. 5C-D.

Performance on the Bacteria Dataset. Table 2 shows the performance of PhaseD2NN on the bacteria dataset. The model performed much better than GPC (SSIM margin = 0.32), but was comparable to that of the LFF (SSIM margin = 0.01). Qualitative results are shown in Fig. 5E.

3. Discussion

3.1. Interpreting the Learned Fourier Filter compared to GPC

We perform a comparison of our learned Fourier filters with the filters implemented by the GPC method as shown in Fig. 3. Considering our learned filters on the HeLa dataset in comparison to the filters from the GPC method, it is evident that the amplitudes of the transmission coefficients are unity across the circular region for the learnable Fourier filter and GPC initialized filter experiments. Furthermore, the phase coefficients of the filters have learnt a structure similar to the GPC filter which consists of a central region enabling a reference beam, and an outer region even after randomly initializing the filter coefficients during training (filters marked with blue shapes). The outer region of the learnt phase coefficients differ for the three datasets due to the different frequency content in each dataset.

Furthermore, note the learnt amplitude coefficients of the filters for the LFF and LFF + GPC init experiments (marked with blue and pink colored shapes). For the Phase MNIST and Bacteria datasets the amplitude coefficients have a degree of attenuation compared to that for the HeLa datasets. We interpret that this behavior is due to the sparsity of the phase objects of the three datasets. Phase MNIST and Bacteria images have large background regions with zero phase. The output intensity image should thus create this background through destructive interference. To achieve destructive interference the amplitude of the object and the reference arms of the filter should be carefully balanced. In our method the filter learns to attenuate each frequency band so that self-interference can generate large dark regions with destructive interference. In contrast GPC filter is incapable of generating the dark background as depicted in Fig. 3-B3,E3. However, for the experiments with \mathcal{L}_{LT} loss, the amplitude coefficients have learnt a considerable pattern for all datasets (marked with orange colored shapes). Here the loss function relaxes reconstruction intensity range from having to be in $[0, 1]$. This seems to enable the filter to further fine-tune to the particular dataset. Our results clearly show that an improved reconstruction (beyond GPC) can be obtained for each dataset by appropriately learning the outer region of the Fourier filter.

Next, we experimented on the effect of the central region in our filters. We removed the outer regions' patterns (on both phase and amplitude) and considered only the central regions. The modified filter still achieved 35%-64% of the original

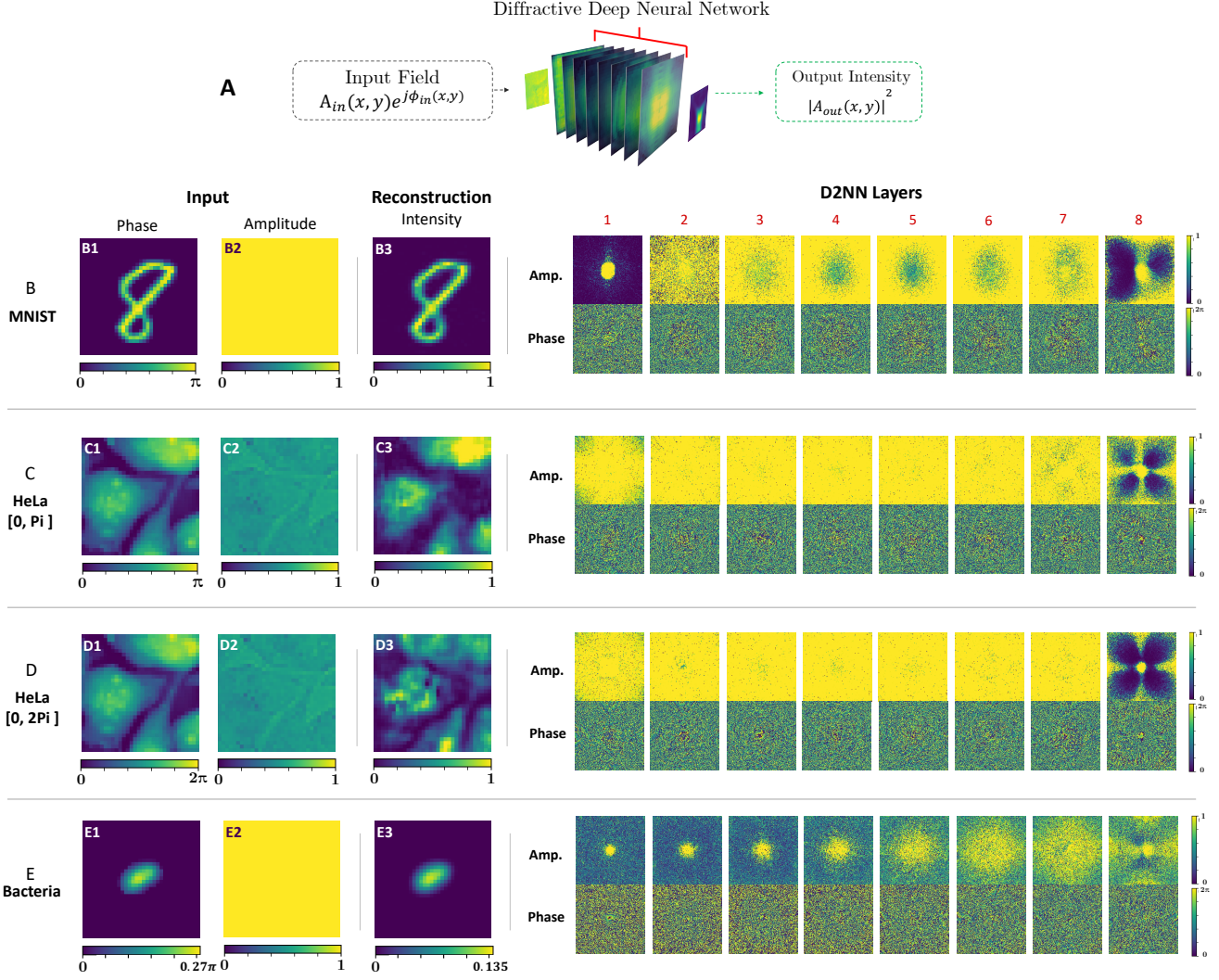


Figure 5. **PhaseD2NN for or all-optical phase to intensity conversion.** (A) The schematic of the PhaseD2NN with eight diffractive layers. (B) The input phase map (B1), the input amplitude map (B2), the reconstructed intensity map (B3), for a representative test image from the Phase MNIST data set. Shown on the right are the learned PhaseD2NN layers trained on the Phase MNIST data set. (C) Similar results as in ‘B’ for the HeLa $[0, \pi]$ data set (D) Similar results as in ‘B’ for the HeLa $[0, 2\pi]$ data set. (E) Similar results as in ‘B’ for the Bacteria dataset. These results show that PhaseD2NN works well for simple data sets such as the MNIST digits and bacteria. For the HeLa data sets the reconstructions should be improved.

SSIM value (supplementary section C.1) on the validation data. This demonstrated that the behavior introduced by the central region of the learned filters is still important and similar to the filters from the GPC method [22].

Moreover, the learned filters for a particular dataset will not essentially generalize for other datasets. To address generalization, we conducted an experiment which can learn a generalized filter for sparse and dense noise datasets separately (see supplementary section C.2). The results are not as impressive since a generalized *linear* operation for the task does not exist (in agreement with Eq. 3.14 in chapter 3 of [22]). It depicts that the mapping from phase to intensity is a spatial-feature-depended approximation on the data distribution.

3.2. Overall Comparison

Fig. 6 summarizes the best reconstruction results achieved by the GPC, learnable Fourier filter (LFF), and the PhaseD2NN in comparison to the empirical upperbounds set by the complex-valued CNN. As noted before, for the fairest SSIM com-

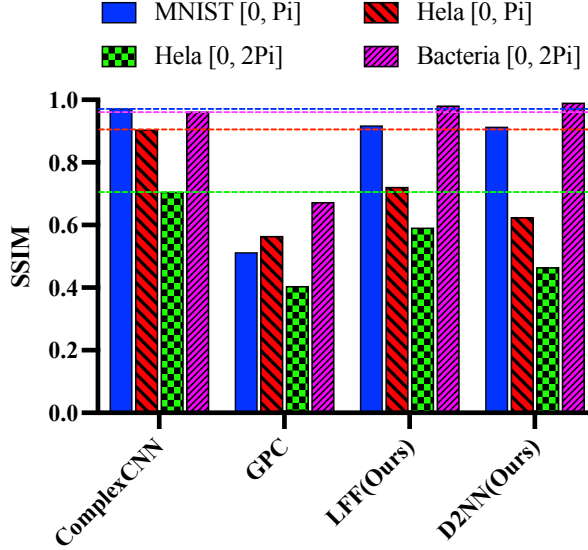


Figure 6. **Comparison of $\partial\mu$ architectures on different datasets.** Our approach significantly outperforms the GPC [22] for all datasets. The dotted lines indicate the empirical upper bounds set by the complex-valued CNN for each dataset.

parison, the output intensity range of the GPC method was scaled for each dataset (see supplementary section B.1.3). On all datasets, LFF and PhaseD2NN outperformed the GPC method. Furthermore, LFF and PhaseD2NN were comparable on MNIST and bacteria data sets. For the HeLa datasets LFF outperformed PhaseD2NN. This result suggests that a single diffractive layer, when placed right, can perform on par with a diffractive deep neural network (D2NN). This is because, though comprised of many layers, a D2NN is a cascade of linear operators that collapses to a single linear operation. The cascading is needed in the spatial domain to connect all pixels; but the same can be achieved by the Fourier operator. In fact, Fourier operator fully-connects the network while D2NN is partially connected. This maybe why LFF outperformed PhaseD2NN on HeLa datasets. However, compared to LFF, PhaseD2NN seems to better generalize to new data distributions. Nevertheless, both LFF and PhaseD2NN have room to improve; neither model reached the empherical upperbounds set by the complex-valued CNN for MNIST and HeLa datasets.

In terms of applicability, our proposed methods accurately converts phase to intensity within the limited phase range $[0, \pi]$. Most biological phase objects would not usually exceed π phase shift. For instance, at $\lambda = 633$ nm wavelength, a $h = 10\mu\text{m}$ thick cell, in a $\Delta n = 0.03$ refractive index difference medium, would generate a maximum $\phi = [2\pi(\Delta n)h]/\lambda = \pi$ rad phase shift [23]. Thus our learned architectures are of practical use in quantitative phase microscopy.

3.3. Limitations and future work

First, all our models performed relatively poorly on dense-feature-rich HeLa datasets. However, this does not necessarily mean that the results are not quantitative. We hope to analyze the optical behavior and improve the reconstruction of complex features as part of our future work. Second, both our all optical methods are linear. Thus D2NN’s multiple layer architecture is of limited use (to the best of our knowledge, we are the first to comprehensively benchmark the limitations of D2NNs due to their linearity). An important future direction is to build non-linear D2NNs that can harness the true power of cascaded diffractive layers. Third, while we have focused on an all-optical system in this work, we believe that the phase-to-intensity reconstruction quality can be further improved by cascading optics with electronic hardware while keeping a fine balance of the computational workload between them. Last, phase to intensity conversion is only a first demonstration of differentiable microscopy ($\partial\mu$). $\partial\mu$ may find use in many other optical design problems when the task can be embedded in data and the cost objective.

4. Conclusion

The current paradigm within microscopy is to develop the system hardware for a specific microscope (e.g. quantitative phase microscope) and then use that for different applications. Here, we propose to change the paradigm by introducing the concept of differentiable microscopy ($\partial\mu$) that can learn the optical imaging process required for a given technical

specification (e.g., extracting phase information) and for different targeted applications. As a first demonstration of $\partial\mu$ we learned all-optical designs for quantitative phase microscopy (QPM).

In conventional QPM, the imaging pipeline is all optical, but the imaging reconstruction require computation resources. Our learnt microscopes completely remove the need of post-imaging computations resources and has a huge potential of making the footprint of microscope compact. In addition, this is the first demonstration of all optical phase-to-intensity conversion through D2NNs. We believe this work will motivate researchers to exploit our designs for applications where high-speed, high-throughput, and compact set-ups are needed. For instance our designs may find use in point-of-care systems in microbiology [24], histopathology [25] and material sciences [26]. Moreover, the proposed all-optical phase-to-intensity conversion can be exploited for applications beyond microscopy, such as for two-photon-polymerization based nano-fabrication [22] and optogenetics [27].

We also think, our work is transformative in physics-based machine learning. Our approach can be uniquely interpretable. Notably, one of our learnt designs is similar to the generalized phase (GPC) concept [22]. Thus, our demonstration is perhaps the first time a machine-learning algorithm learnt a sophisticated interferometry concept. It would be interesting to see if $\partial\mu$ can invent well known microscope designs from data for various other tasks (such as for depth-resolved imaging or for optical coherence tomography). We anticipate that differentiable microscopy will open doors to a new generation of interdisciplinary scientists, to design novel optical systems for challenging imaging problems.

5. Materials and Methods

5.1. Datasets:

For the experiments, we have considered the following datasets.

Phase MNIST Digits. To preserve consistency with existing studies [18] we consider the *Phase MNIST digit* dataset for evaluation. To construct this dataset, we convert the images from the MNIST digit dataset to phase images ($e^{j\phi_{in}}$) such that $\phi_{in} \in [0, \pi]$. The dataset contains 50000, 5000, 5000 train, validation, test images respectively.

We considered this dataset as a *sparse dataset* because it contains relatively less complex structures (e.g. Contains only a single digit located at the center of the image grid)

HeLa Dataset. To evaluate the proposed method on microscopy, we acquire a dataset of *HeLa* cells where the samples are illuminated with 600 nm light. Dataset contains 10344 images where each image represents a complex field. 80%, 10%, 10% of the dataset are utilized for training, validation, test sets respectively.

The electric field amplitudes are normalized to $[0, 1]$ based on the maximum amplitude obtained through the steps described in Section 5.3. To remove outliers in the phase, values are clipped to $[0, 2\pi]$. To study the effect of the distribution of phase values in a limited range, the phase information of the above dataset is re-scaled to $[0, \pi]$ and considered as a separate dataset for reporting performance.

Bacteria Dataset. This is another acquired dataset for the purpose of evaluating the network performances for microscopy. The dataset has phase information $\phi_{in} \in [0, 2\pi]$. This can also be considered as a *sparse dataset* similar to the Phase MNIST dataset.

Phase Noise Dataset. We created different phase noise datasets for two sparsity levels for the evaluation of the generalizability of learnable Fourier filter. These datasets are named *Sparse noise dataset* and *Dense noise dataset*. The amplitude of the noise images are set to unity while the phase (ϕ_{in}^{noise}) is sampled from standard normal distribution.

Algorithm 1 shows the procedure to generate noise datasets for different sparsity levels. p_{thresh} is the noise sparsity level. We set $p_{thresh} = 0.1$ and $p_{thresh} = 0.9$ for the sparse and dense noise datasets respectively. Furthermore, to cover a wide range of sparsity levels we generated a third dataset called the *Wide noise dataset* with a similar phase and amplitude setup, however with p_{thresh} set to values within the range $[0.1, 1.0]$ with increments of 0.1.

5.2. Sample Preparation:

HeLa cells. HeLa cells were grown in a standard humidified incubator at 37 °C with 5% CO₂ in minimum essential medium supplemented with 1% penicillin/streptomycin and 10% fetal bovine serum. Cells were seeded into the Polydimethylsiloxane

Algorithm 1 Generating noise dataset with different sparsity levels

```
for  $\phi(x, y)$  in  $\phi_{in}^{noise}$  do
  if  $\phi(x, y) \geq p_{thresh}$  then
     $\phi(x, y) = 0$ 
  end if
end for
```

chamber of $10\text{ mm} \times 10\text{ mm}$ size with $150\text{ }\mu\text{m}$ thickness on a reflecting silicon substrate. The cells were left in the incubator for 1-2 days for their growth in a densely packed manner and fixed for ~ 20 min using 4% paraformaldehyde in phosphate buffered saline. The sample is then sealed with # 1.5 cover glass from the top which enabled to use water immersion objective lens for imaging and also avoided any air current in the specimen.

Bacteria. Bacteria samples has Brownian motion due to their small sizes, which introduce challenges in imaging them using a multi-shot QPM system. Multi-shot QPM acquires multiple interferometric frames for the phase recovery and therefore specimen should be immobile within the multi frame acquisition time. The bacteria samples were also prepared on a reflecting substrate (Si-wafer) due to the reflection geometry of our optical setup. First, the substrate was thoroughly washed with dist. H₂O and dried with N₂ gas. The 2-polydimethylsiloxane (PDMS) chamber of opening $10 \times 10\text{ mm}$ was placed on top of Si-wafer and the opening area is filled with poly-L-lysine (PLL). The substrate is incubated with PLL for 15-20 minutes and then access amount of PLL is removed and gently washed using phosphate-buffered saline (PBS). The thin layer of PLL positively charges the Si-wafer surface and helps to adhere the negatively charge bacteria cells for imaging. The $20 - 25\text{ }\mu\text{l}$ volume of bacteria sample is pipetted in the PDMS chamber and left for 30 minutes of incubation. The bacteria cells were adhered to the surface of Si-wafer due to the electrostatic attraction between the negatively charged bacteria and positively charged wafer surface. The immobile bacteria cells were further gently washed off with PBS and covered with # 1.5 cover glass from the top to use high resolution water immersion objective lens ($60\times/1.2\text{NA}$) for imaging.

5.3. Quantitative Phase Imaging:

For quantitative phase imaging, HeLa sample is placed under the Linnik interferometer based quantitative phase microscopy (QPM), which works on the reflection mode. The sample is illuminated with partially spatial and highly temporal coherent light source also called pseudo-thermal light source to generate high quality interferometric images. This light source illumination has unique advantages such as high spatial and temporal resolution, high spatial phase sensitivity, extended range of optical path difference adjustment between the interferometric arms etc over conventional light sources, e.g., lasers, white light, and light emitting diodes [25]. More details of the experimental setup can be found in previous work [25]. The imaging of HeLa cells is performed using high resolution water immersion objective lens ($60\times/1.2\text{NA}$) at 660 nm wavelength. This provided the theoretical transverse resolution approximately equal to 275 nm , which is quite good for high resolution phase recovery of the specimens. The interferometric data is recorded with 5.3 Megapixels ORCA-Fusion digital CMOS camera (model # C14440-20UP). The camera sensor has 2304×2304 pixels with $6.5\text{ }\mu\text{m}$ pixel size and provided fairly big $225\text{ }\mu\text{m} \times 225\text{ }\mu\text{m}$ FOV at $60\times$ optical magnification in QPM system. We acquired approximately 500 such FOVs of different region of interests of the HeLa sample and each FOV contained roughly 50 – 60 cells. For bacteria samples, more than 50 FOVs of different regions of interests were found to be sufficient to generate large amount of interferometric data due to their small sizes compared to HeLa cells. Each FOVs contained more than 500 bacteria cells and thus provided approximately 25000 bacteria cells interferometric images for machine learning. The recorded interferometric images are further post processed with random phase-shifting algorithm based on principal component analysis [28] for the recovery of the complex fields related to HeLa cells.

References

- [1] John P. Wourms. Light Microscopy: Renaissance and Revolution. *BioScience*, 40(5):397–399, 5 1990. 1
- [2] Jongchan Park, David J. Brady, Guoan Zheng, Lei Tian, and Liang Gao. Review of bio-optical imaging systems with a high space-bandwidth product. *Advanced Photonics*, 3(04):1–18, 2021. 1
- [3] Yujia Xue, Shiyi Cheng, Yunzhe Li, and Lei Tian. Reliable deep-learning-based phase imaging with uncertainty quantification. 2019. 1
- [4] Hongda Wang, Yair Rivenson, Yiyin Jin, Zhensong Wei, Ronald Gao, Harun Günaydin, Laurent A. Bentolila, Comert Kural, and Aydogan Ozcan. Deep learning enables cross-modality super-resolution in fluorescence microscopy. *Nature Methods*, 16(1), 2019. 1

- [5] Colin L. Cooke, Fanjie Kong, Amey Chaware, Kevin C. Zhou, Kanghyun Kim, Rong Xu, D. Michael Ando, Samuel J. Yang, Pavan Chandra Konda, and Roarke Horstmeyer. Physics-enhanced machine learning for virtual fluorescence microscopy. In *Proceedings of the IEEE/CVF International Conference on Computer Vision (ICCV)*, pages 3803–3813, 2021. 1
- [6] Ayan Chakrabarti. Learning sensor multiplexing design through back-propagation. *Advances in Neural Information Processing Systems*, (Nips):3089–3097, 2016. 1
- [7] He Sun, Adrian V. Dalca, and Katherine L. Bouman. Learning a probabilistic strategy for computational imaging sensor selection. *IEEE International Conference on Computational Photography, ICCP 2020*, 2020. 1
- [8] Amey Chaware, Colin L. Cooke, Kanghyun Kim, and Roarke Horstmeyer. Towards an intelligent microscope: Adaptively learned illumination for optimal sample classification. *ICASSP, IEEE International Conference on Acoustics, Speech and Signal Processing - Proceedings*, 2020-May:9284–9288, 2020. 1
- [9] Alex Muthumbi, Amey Chaware, Kanghyun Kim, Kevin C. Zhou, Pavan Chandra Konda, Richard Chen, Benjamin Judkewitz, Andreas Erdmann, Barbara Kappes, and Roarke Horstmeyer. Learned sensing: jointly optimized microscope hardware for accurate image classification. *Biomedical Optics Express*, 10(12):6351, 2019. 1
- [10] Roarke Horstmeyer, Richard Y. Chen, Barbara Kappes, and Benjamin Judkewitz. Convolutional neural networks that teach microscopes how to image. 2017. 1
- [11] Kanghyun Kim, Pavan Chandra Konda, Colin L. Cooke, Ron Appel, and Roarke Horstmeyer. Multi-element microscope optimization by a learned sensing network with composite physical layers. *Optics Letters*, 45(20):5684, 2020. 1
- [12] Hassaan Majeed, Shamira Sridharan, Mustafa Mir, Lihong Ma, Eunjung Min, Woonggyu Jung, and Gabriel Popescu. Quantitative phase imaging for medical diagnosis. *Journal of Biophotonics*, 10(2):177–205, 2017. 2
- [13] Mustafa Mir, Huafeng Ding, Zhuo Wang, Jason Reedy, Krishnarao Tangella, and Gabriel Popescu. Blood screening using diffraction phase cytometry. *Journal of Biomedical Optics*, 15(2), 2010. 2
- [14] Darina Roitshtain, Lauren Wolbromsky, Evgeny Bal, Hayit Greenspan, Lisa L. Satterwhite, and Natan T. Shaked. Quantitative phase microscopy spatial signatures of cancer cells. *Cytometry Part A*, 91(5):482–493, 2017. 2
- [15] Pierre Marquet, Christian Depeursinge, and Pierre J. Magistretti. Review of quantitative phase-digital holographic microscopy: promising novel imaging technique to resolve neuronal network activity and identify cellular biomarkers of psychiatric disorders. *Neurophotonics*, 1(2), 2014. 2
- [16] Chenfei Hu and Gabriel Popescu. Quantitative phase imaging (QPI) in neuroscience. *IEEE Journal of Selected Topics in Quantum Electronics*, 25(1):1–9, 2019. 2
- [17] Jesper Glückstad. Phase contrast image synthesis. *Optics Communications*, 130(4-6):225–230, 1996. 2, 3, 1
- [18] Xing Lin, Yair Rivenson, Nezh T. Yardimci, Muhammed Veli, Yi Luo, Mona Jarrahi, and Aydogan Ozcan. All-optical machine learning using diffractive deep neural networks. *Science*, 361(6406), 2018. 2, 11, 1
- [19] Laurent Zwald and Sophie Lambert-Lacroix. The BerHu penalty and the grouped effect. 2012. 3
- [20] Deniz Mengu, Muhammed Veli, Yair Rivenson, and Aydogan Ozcan. Classification and reconstruction of spatially overlapping phase images using diffractive optical networks. pages 1–30, 8 2021. 3, 2
- [21] Chiheb Trabelsi, Olexa Bilaniuk, Ying Zhang, Dmitriy Serdyuk, Sandeep Subramanian, Joao Felipe Santos, Soroush Mehri, Negar Rostamzadeh, Yoshua Bengio, and Christopher J Pal. Deep complex networks. In *International Conference on Learning Representations*, 2018. 3
- [22] Jesper Glückstad and Darwin Palima. Generalized phase contrast. *Springer Series in Optical Sciences*, 146:7–12, 2009. 9, 10, 11, 1, 2, 7
- [23] Yongjin Sung, Wonshik Choi, Christopher Fang-Yen, Kamran Badizadegan, Ramachandra R. Dasari, and Michael S. Feld. Optical diffraction tomography for high resolution live cell imaging. *Optics InfoBase Conference Papers*, 17(1):1977–1979, 2009. 10
- [24] Youngju Jo, Jaehwang Jung, Jee Woong Lee, Della Shin, Hyunjo Park, Ki Tae Nam, Ji Ho Park, and Yongkeun Park. Angle-resolved light scattering of individual rod-shaped bacteria based on Fourier transform light scattering. *Scientific Reports*, 4:1–6, 2014. 11
- [25] Azeem Ahmad, Vishesh Dubey, Nikhil Jayakumar, Anowarul Habib, Ankit Butola, Mona Nystad, Ganesh Acharya, Purusotam Basnet, Dalip Singh Mehta, and Balpreet Singh Ahluwalia. High-throughput spatial sensitive quantitative phase microscopy using low spatial and high temporal coherent illumination. *Scientific Reports*, 11(1):15850, 2021. 11, 12
- [26] Renjie Zhou, Chris Edwards, Gabriel Popescu, and Lynford Goddard. Semiconductor defect metrology using laser-based quantitative phase imaging. *Quantitative Phase Imaging*, 9336(March 2015):93361I, 2015. 11
- [27] Jesper Glückstad, RenéL. Eriksen, and Andreas Gejl Madsen. GPC-modalities for neurophotonics and optogenetics. International Society for Optics and Photonics, SPIE, 2021. 11

- [28] J. Vargas, J. Antonio Quiroga, and T. Belenguer. Phase-shifting interferometry based on principal component analysis. *Opt. Lett.*, 36(8):1326–1328, Apr 2011. [12](#)
- [29] Yair Rivenson, Tairan Liu, Zhensong Wei, Yibo Zhang, Kevin de Haan, and Aydogan Ozcan. PhaseStain: the digital staining of label-free quantitative phase microscopy images using deep learning. *Light: Science and Applications*, 8(1), 2019. [1](#)
- [30] Yoav N. Nygate, Mattan Levi, Simcha K. Mirsky, Nir A. Turko, Moran Rubin, Itay Barnea, Gili Dardikman-Yoffe, Miki Haifler, Alon Shalev, and Natan T. Shaked. Holographic virtual staining of individual biological cells. *Proceedings of the National Academy of Sciences of the United States of America*, 117(17), 2020. [1](#)
- [31] Yair Rivenson, Yibo Zhang, Harun Günaydin, Da Teng, and Aydogan Ozcan. Phase recovery and holographic image reconstruction using deep learning in neural networks. *Light: Science and Applications*, 7(2), 2018. [1](#)
- [32] Ayan Sinha, Justin Lee, Shuai Li, and George Barbastathis. Lensless computational imaging through deep learning. *Optica*, 4(9), 2017. [1](#)
- [33] Michael Kellman, Emrah Bostan, Michael Chen, and Laura Waller. Data-Driven Design for Fourier Ptychographic Microscopy. *2019 IEEE International Conference on Computational Photography, ICCP 2019*, pages 2–9, 2019. [1](#)
- [34] Michael R. Kellman, Emrah Bostan, Nicole A. Repina, and Laura Waller. Physics-Based Learned Design: Optimized Coded-Illumination for Quantitative Phase Imaging. *IEEE Transactions on Computational Imaging*, 5(3), 2019. [1](#)
- [35] Julie Chang, Vincent Sitzmann, Xiong Dun, Wolfgang Heidrich, and Gordon Wetzstein. Hybrid optical-electronic convolutional neural networks with optimized diffractive optics for image classification. *Scientific Reports*, 8(1):1–10, 2018. [1](#)
- [36] Carlos Mauricio Villegas Burgos, Tianqi Yang, Yuhao Zhu, and A. Nickolas Vamivakas. Design framework for metasurface optics-based convolutional neural networks. *Applied Optics*, 60(15):4356, 2021. [1](#)
- [37] Shane Colburn, Yi Chu, Eli Shilzerman, and Arka Majumdar. Optical frontend for a convolutional neural network. *Applied Optics*, 58(12):3179, 4 2019. [1](#)
- [38] Qiuha Wu, Xiubao Sui, Yuhang Fei, Chen Xu, Jia Liu, Guohua Gu, and Qian Chen. Multi-layer optical Fourier neural network based on the convolution theorem. *AIP Advances*, 11(5):1–6, 2021. [1](#)
- [39] F. Zernike. Phase contrast, a new method for the microscopic observation of transparent objects. *Physica*, 9(7), 1942. [1](#)
- [40] F. Zernike. Phase contrast, a new method for the microscopic observation of transparent objects part II. *Physica*, 9(10), 1942. [1](#)
- [41] Linmei Li, Shiqiang Yan, Bingcheng Lin, Qihui Shi, and Yao Lu. *Single-Cell Proteomics for Cancer Immunotherapy*, volume 139. Elsevier Inc., 1 edition, 2018. [1](#)
- [42] Jingxi Li, Deniz Mengü, Yi Luo, Yair Rivenson, and Aydogan Ozcan. Class-specific differential detection in diffractive optical neural networks improves inference accuracy. *Advanced Photonics*, 1(04), 2019. [1](#)
- [43] Tao Yan, Jiamin Wu, Tiankuang Zhou, Hao Xie, Feng Xu, Jingtao Fan, Lu Fang, Xing Lin, and Qionghai Dai. Fourier-space Diffractive Deep Neural Network. *Physical Review Letters*, 123(2), 2019. [1](#)
- [44] Yi Luo, Deniz Mengü, Nezh T. Yardimci, Yair Rivenson, Muhammed Veli, Mona Jarrahi, and Aydogan Ozcan. Design of task-specific optical systems using broadband diffractive neural networks. *Light: Science and Applications*, 8(1):1–14, 2019. [1](#)
- [45] Md Sadman Sakib Rahman and Aydogan Ozcan. Computer-Free, All-Optical Reconstruction of Holograms Using Diffractive Networks. *ACS Photonics*, page acsphotronics.1c01365, 10 2021. [2](#)
- [46] J.W. Goodman. *Introduction to Fourier Optics*. Electrical Engineering Series. McGraw-Hill, 1996. [2](#), [3](#), [4](#), [5](#)
- [47] J. A. Ratcliffe. Some Aspects of Diffraction Theory and their Application to the Ionosphere. *Reports on Progress in Physics*, 19(1):306, 1 1956. [4](#)

Differentiable Microscopy Designs an All Optical Quantitative Phase Microscope

Supplementary Material

A. Related Work

Image Reconstruction through Post-processing. Commonly, images acquired from microscopy techniques need processing before they can be used for desired tasks. In the context of phase imaging, deep learning has shown promise in improving microscopy techniques through the post-processing of acquired images. These methods approximate the inverse function of imaging models and have applications such as virtual staining [29, 30] and phase retrieval [31, 32].

Optical Hardware Optimization. Rather than following the static optical setup of the microscope and post-processing its acquired images, recent methods have focused on optimizing certain parts of the optical hardware itself. Several approaches focus on optimizing the illumination patterns of the microscope [8–11]. This research direction of jointly optimizing the forward optics (by learning illumination patterns) with the inverse reconstruction model has been able to reduce the data requirement in QPM [33, 34]. However, since the focus is only on the *illumination aspect*, the extent to which the forward optics model can be optimized is constrained. In contrast, in differentiable microscopy ($\partial\mu$), here we focus on learning new optical systems, and interpretable design rules.

Fourier Plane Filter Optimization. The 4- f optical system (Fig. 1(a)) produces the Fourier transform of the incident spatial light at the Fourier plane. This Fourier transform property of a lens can be leveraged to perform the convolution operation through light itself by placing filters at the Fourier plane. The effectiveness of this optical convolution has been studied in the literature to perform various classification tasks [35–38].

All-Optical Phase Retrieval Methods. The work of Zernike [39, 40] paved the way to clearly visualize transparent biological samples under a microscope without applying contrast dyes onto the specimen. Thus, the development of phase contrast microscopy is a significant milestone in biological imaging. This phase contrast method is implemented in a common-path interferometer where the signal and reference beams resulting from the illumination travel along the same optical axis and interfere at the output of the optical system generating an interferogram. The phase perturbations introduced by the optical characteristics (refractive index, thickness) of the object are converted to observable intensity variations on the interferogram, by the use of a Fourier plane filter in the optical path. This filter functions as a phase shifting filter which imparts a quarter-wave shift on the undiffracted light components (the reference beam). However, the linear relationship between the input phase and output intensity of this system is derived based on the “small-scale” phase approximation, where the largest input phase deviation is considered to be $\pi/3$. Glückstad [17] generalized Zernike’s phase contrast method and introduced the generalized phase contrast (GPC) method to provide an all-optical linear phase to intensity conversion approach, which overcomes the restriction of “small-scale” phase approximation. The descriptive mathematical analysis of the filter implementation in [22] shows the utilization of a phase shifting Fourier plane filter, where its parameters are carefully selected to appropriately generate the synthetic reference wave (SRW) to reveal the input phase perturbations in the output interference pattern. Through further mathematical analysis they have demonstrated how the system parameters can be optimized to produce accurate phase variation measurements and reduce the error in quantitative phase microscopy when a GPC-based method is utilized with post-processing. Even though the GPC method is capable of linearly mapping the input phase information to the output intensity all optically, it requires a careful mathematical analysis, a considerable amount of domain knowledge and relatively complex optical setups with post-processing to implement quantitative phase imaging. On the other hand, in our implementation the microscope is optimized for phase reconstruction as an end-to-end differentiable model.

Diffractive Deep Neural Networks. D2NNs are a type of optical neural networks which is introduced by Lin *et al.* [18] as a physical mechanism to perform machine learning. They consist of a set of diffractive surfaces acting as the layers of the machine learning model. The transmission coefficients of each diffractive element act as the neurons of the network and they can be trained by modelling them with optical diffraction theory. The trained diffraction surfaces can be 3D printed and inference is done by propagating light through the D2NN. Since they work purely optically, the D2NNs has the capability of performing computations at the speed of light with no power consumption. D2NNs are utilized for various tasks such as image classification [41, 42], object detection and segmentation [43], designing task-specific optical systems [44], reconstruction

of overlapping phase objects [20], and image reconstruction using holograms [45]. In contrast to this, we utilize the D2NN for the direct phase to intensity conversion. Our method is the first demonstration of phase-to-intensity conversion through D2NNs to the best of our knowledge.

B. Mathematical Modelling of Optical Systems

B.1. Learnable Fourier Filter Based Model

B.1.1 4- f system

Fig. S1 shows the system which is generally referred to as 4- f filtering architecture [46]. It is referred as 4- f because of the distance between the input plane (P_1) and the image plane (P_3) equals to $4 \times f$, where f is the focal length of the lenses. Here S is the point source, P_1, P_2, P_3 are the input plane, Fourier plane and the image plane, respectively, and L_1, L_2, L_3 are identical lenses each having a focal length f . The light from S is collimated with the lens L_1 . The input sample (P_1) which has $g(x_1, y_1)$ amplitude transmission coefficient is placed against L_1 to reduce the overall length of the system. The resultant light is then collimated with the Fourier transforming lens L_2 resulting $k_1 G(\frac{x_2}{\lambda f}, \frac{y_2}{\lambda f})$ field at P_2 plane where G is the Fourier transform of g and k_1 is a constant. To manipulate the spectrum of input field $g(x_1, y_1)$, filter can be placed in the Fourier plane in P_2 . The transmission coefficient of the filter is given by

$$t_A(x_2, y_2) = k_2 H\left(\frac{x_2}{\lambda f}, \frac{y_2}{\lambda f}\right), \quad (1)$$

if the desired frequency domain transfer function is H and k_2 is a constant. Following lens L_3 applies the Fourier transform again on the modified spectrum to obtain the inverted modified field.

B.1.2 GPC-based Initialization

The GPC introduced by Glückstad [22] is a circular filter in the Fourier plane consisting of 2 main regions, namely; the central region and the outer region. In this implementation, a phase shift is introduced by the central region of the filter which results in an interference pattern that produces a substantial contrastive image of the input phase object. Therefore, with the goal of improving the performance of the existing filter, rather than randomly initializing the filter weights, we initialized the weights with the GPC filter parameters to train the network. After experimenting with different filter combinations on the datasets (supplementary section 5.1) we selected the GPC transmission coefficients to have unit amplitude, $\pi/2$ phase shift in the central region and, 0 phase shift in the outer region.

B.1.3 Scaling the Reconstruction of the GPC Method

After designing the GPC filter as described in section B.1.2, since the GPC method does not naturally reconstruct the output intensity (*out*) within the $[0, 1]$ range, it is required to select the appropriate scaling factor S for the filter reconstructions. This is done since our methods are trained to reconstruct the output intensity within $[0, 1]$ range for comparison purposes. Therefore, we search the suitable S for the GPC reconstructions for a subset of the train set of each dataset, so that it can be scaled to obtain the best SSIM value as shown in eq. (2) for an intensity reconstruction within the $[0, 1]$ range.

$$SSIM_{best} = \arg \max_S SSIM((S * out), gt_{angle}) \quad (2)$$

B.2. A Brief Review of Diffractive Deep Neural Networks

A D2NN comprises of a set of diffractive layers. Each diffractive element (neuron) in a diffractive layer can be considered as a secondary wave source according to the Huygens-Fresnel principle [18]. The diffraction at each neuron can be modelled using the Rayleigh-Sommerfeld diffraction formulation [46, ch. 3.5] as follows.

The Rayleigh-Sommerfeld diffraction theory describes the diffraction of light by an aperture in an infinite opaque planar screen. Consider such an aperture illuminated by a light wave which has a field $U(P_1)$ at a point $P_1 \equiv (x_1, y_1, z_1)$ on the aperture surface S as shown in Fig. S2.

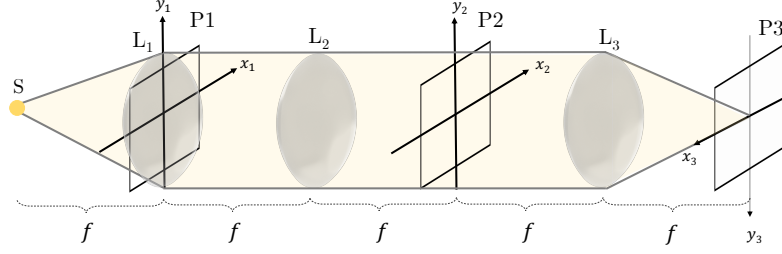


Figure S1. 4- f system

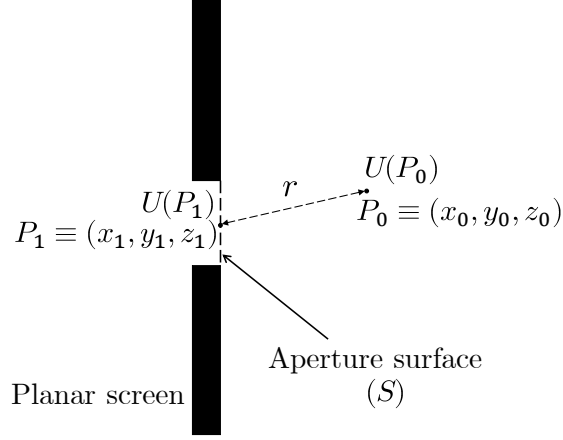


Figure S2. Diffraction by an aperture in a planar screen.

The field at point $P_0 \equiv (x_0, y_0, z_0)$ after the diffraction can be given using the first Rayleigh-Sommerfeld solution to the diffraction problem, which is given as

$$U(P_0) = \iint_S U(P_1) \left(\frac{z_0 - z_1}{r^2} \right) \left(\frac{1}{2\pi r} + \frac{1}{j\lambda} \right) e^{j\frac{2\pi r}{\lambda}} dS. \quad (3)$$

Here, $r = \sqrt{(x_0 - x_1)^2 + (y_0 - y_1)^2 + (z_0 - z_1)^2}$ is the distance between the points P_1 and P_0 , λ is the wavelength of the light wave and $j = \sqrt{-1}$. This integral holds under the conditions that, U is a homogeneous scalar wave equation and it satisfies the *Sommerfeld radiation condition* which states that U must vanish at least as fast as a diverging spherical wave [46, ch. 3.4].

B.2.1 Mathematical Modelling of D2NNs

The integral in eq. (3) can be directly converted to a Riemann summation considering a discrete set of sampling points on the aperture plane. In this direct implementation, each neuron in a diffractive layer is considered as a sampling point.

As shown in Fig. S3, suppose that the field at the i^{th} neuron of the $(l-1)^{\text{th}}$ layer (N_i^{l-1}), which is located at (x_i, y_i, z_{l-1}) is given by U_i^{l-1} , and the diffraction caused at this neuron results in the field given by $U_{m,i}^l$ at N_m^l located at (x_m, y_m, z_l) . Then, $U_{m,i}^l$ is given by,

$$U_{m,i}^l = U_i^{l-1} t_i^{l-1} w_{m,i}^l \Delta A_i^{l-1}, \quad (4)$$

where

$$w_{m,i}^l = \left(\frac{\Delta z}{r_{m,i}^2} \right) \left(\frac{1}{2\pi r_{m,i}} + \frac{1}{j\lambda} \right) \exp \left\{ \left(\frac{j2\pi r_{m,i}}{\lambda} \right) \right\}. \quad (5)$$

Here, ΔA_i^{l-1} is the area of N_i^{l-1} , t_i^{l-1} is the transmission coefficient of the same neuron, λ is the wavelength of the optical wave, $\Delta z = z_l - z_{l-1}$ is the distance between the two adjacent layers along the direction of light propagation,

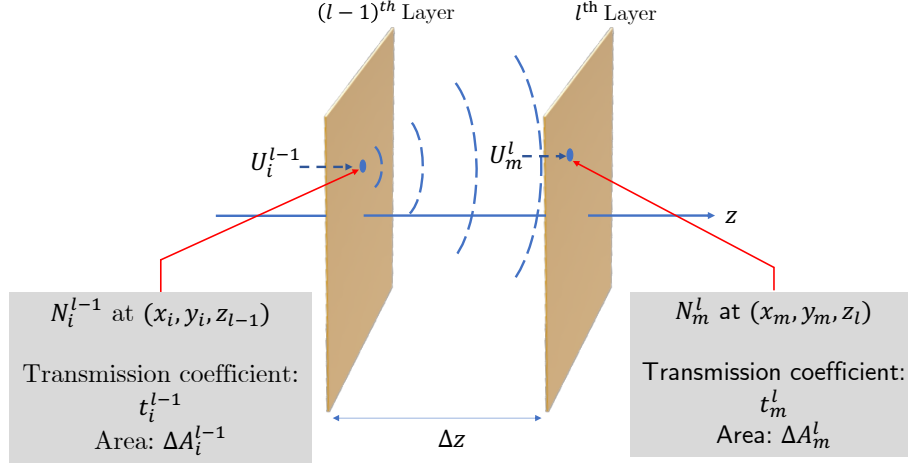


Figure S3. Diffraction of light waves by a neuron of a D2NN layer.

$r_{m,i} = \sqrt{(x_m - x_i)^2 + (y_m - y_i)^2 + \Delta z^2}$, and $j = \sqrt{-1}$. The overall resulting field at N_m^l is the superposition of all the fields resulted by the diffraction at each of the neurons at the $(l-1)^{\text{th}}$ layer which is given by

$$U_m^l = \sum_i U_{m,i}^l. \quad (6)$$

However, direct implementation of these equations results in resource intensive computations in the simulations. A more computationally efficient modelling is done using the fact that the field resulted by an optical wave and its angular spectrum are related through the Fourier transform [46, 47]. This method is known as the angular spectrum (AS) method and it is used for simulating D2NNs in our work.

B.2.2 Angular Spectrum Method

A plane wave can be considered as a combination of a set of plane waves travelling in different directions. The complex amplitudes of these plane wave components form the angular spectrum of the given wave [47]. Consider the field of a light wave propagating in the z direction is given by,

$$U(x, y, z, t) = U(x, y, z) e^{-j2\pi f t}, \quad (7)$$

where f is the temporal frequency of the wave. Suppose that, at $z = 0$ plane, $U(x, y, z)|_{z=0} \equiv U(0)$. It can be shown that the field $U(0)$ and its angular spectrum $A(f_x, f_y, 0) \equiv A(0)$ are related by [47],

$$U(0) = \int_{-\infty}^{\infty} \int_{-\infty}^{\infty} A(0) e^{j2\pi(f_x x + f_y y)} df_x df_y. \quad (8)$$

Here, $f_x = \frac{\alpha}{\lambda}$ and $f_y = \frac{\beta}{\lambda}$, where α and β are direction cosines of the plane wave components with respect to the x and y axes. Note that eq. (8) is of the form of 2-D inverse Fourier transform. Hence, the field and its angular spectrum can be considered as a Fourier transform pair. A generalized form of this result can be written as

$$U(z) \xleftrightarrow{\mathcal{F}} A(z), \quad (9)$$

where $U(z) \equiv U(x, y, z)$ is the field on $z = z$ plane and $A(z) \equiv A(f_x, f_y, z)$ is its angular spectrum. Suppose that the relationship between the angular spectrum at $z = 0$ and $z = z$ planes is given as

$$A(z) = A(0) G(z) \quad (10)$$

where, $G(z) \equiv G(f_x, f_y, z)$ is the propagation transfer function which characterises the propagation of the angular spectrum.

Electromagnetic waves satisfy the Helmholtz equation and therefore $U(z)$ should also satisfy it. This can be used to find an expression for $G(z)$. The Helmholtz equation is given as

$$(\nabla^2 + k^2) U(z) = 0, \quad (11)$$

where $k = \frac{2\pi}{\lambda}$ is the wavenumber which is the magnitude of the propagation vectors $\vec{k} = [k_x, k_y, k_z]$ of the wave components. Considering eq. (9), eq. (10), and eq. (11), it can be observed that $G(z)$ satisfies

$$\frac{d^2 G(z)}{dz^2} + k_z^2 G(z) = 0, \quad (12)$$

where

$$k_z = 2\pi \sqrt{\frac{1}{\lambda^2} - f_x^2 - f_y^2}. \quad (13)$$

An elementary solution to eq. (12) can be written as,

$$G(z) = \exp \left(j2\pi z \sqrt{\frac{1}{\lambda^2} - f_x^2 - f_y^2} \right). \quad (14)$$

Hence, eq. (10) can be re-written as

$$A(z) = A(0) \exp \left(j2\pi z \sqrt{\frac{1}{\lambda^2} - f_x^2 - f_y^2} \right). \quad (15)$$

This equation shows that when $f_x^2 + f_y^2 \leq \frac{1}{\lambda^2}$, the propagation of the angular spectrum along the z axis introduce a different set of phase shift to each of the components of the angular spectrum [46]. However, when $f_x^2 + f_y^2 > \frac{1}{\lambda^2}$, eq. (15) can be written as,

$$A(z) = A(0) \exp \left(-2\pi z \sqrt{f_x^2 + f_y^2 - \frac{1}{\lambda^2}} \right). \quad (16)$$

In this case, the angular spectrum is exponentially attenuated along the z axis. These wave components are known as *evanescent waves* and they do not propagate energy along the z axis.

B.2.3 Implementation of the Angular Spectrum Method

The Fourier relationship between the electric/magnetic field of a light wave and its AS can be obtained using the discrete Fourier transform (DFT) which can be computed efficiently using a fast Fourier transform (FFT) algorithm. Consider two layers of a D2NN at $z = 0$ plane ($(l-1)^{\text{th}}$ layer) and at $z = z_0$ plane (l^{th} layer) as shown in Fig. S4. The input field at the $(l-1)^{\text{th}}$ layer is given by $U(x, y, 0) \equiv U^{l-1}$ and the resulting field at the observation plane is given by $U(x, y, z_0) \equiv U^l$. The width and the height of both layers are L where t^{l-1} and t^l are the complex transmission coefficient matrices of the two layers.

Fig. S5 shows the computation pipeline of the output field using the AS method. Initially, the input field is sampled with a sampling interval of dx in the spatial domain. The sampled input has a size of $N \times N$ samples, where $N = L/dx$. The sampled input is then multiplied element-wise with t^{l-1} to obtain the effective field at the $(l-1)^{\text{th}}$ layer which is given by

$$U_{\text{eff}}^{(l-1)} = U^{l-1} \circ t^{l-1}, \quad (17)$$

where \circ is the element-wise matrix multiplication.

Since the region of support of the input is bounded in the spatial domain, the region of support of its Fourier transform is unbounded and to get a more accurate AS, a higher number of samples of the Fourier transform need to be considered. Therefore, for the computation purposes a separate computational window of the size $wN \times wN$ samples is considered where w is the computation window factor. The oversampling in the Fourier domain is performed by zero padding U_{eff}^{l-1} at the boundary to match the size of the computation window. Then the 2D-DFT of the input field is taken followed by a DFT shift operation to make the center of the computation window $(0, 0)$ resulting the AS given by A^{l-1} .

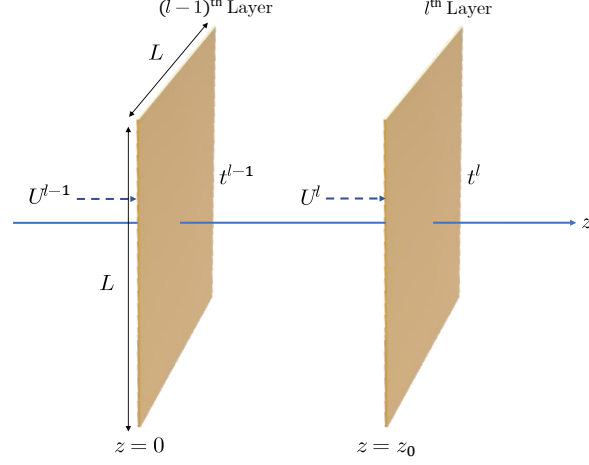


Figure S4. **Two adjacent layers of the D2NN.** The field incident on the $(l-1)^{\text{th}}$ layer is U^{l-1} which is subjected to diffraction at the layer and results the field U^l just before the next layer.

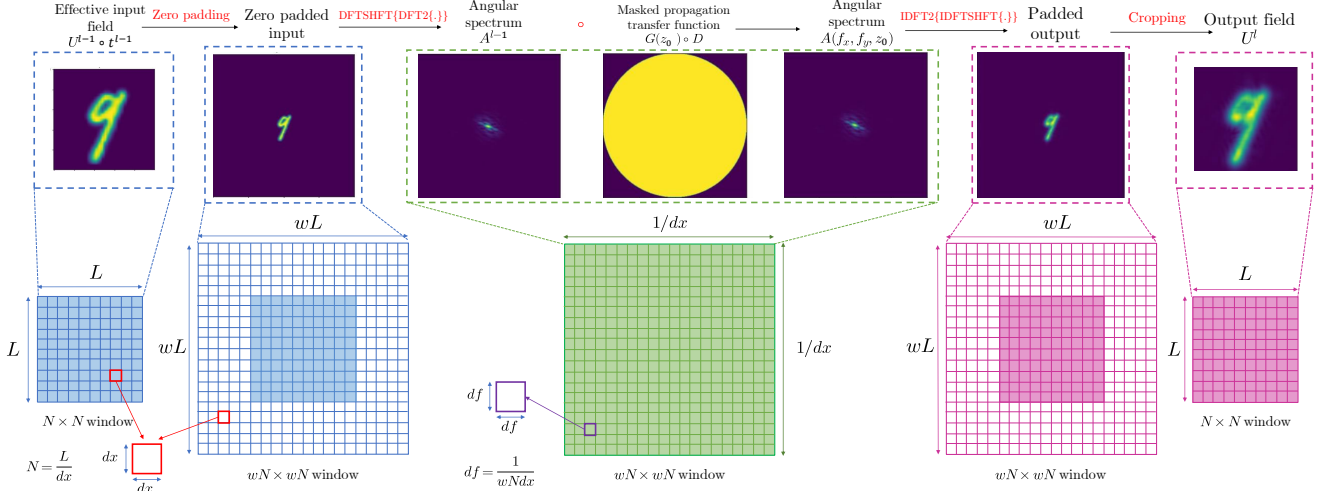


Figure S5. **Computational pipeline of the AS method.** In the figure $DFT2\{\cdot\}$ denotes the 2D-DFT operation, $DFTSHFT\{\cdot\}$ denotes the DFT shift operation, $IDFT2\{\cdot\}$ denotes the 2D-IDFT operation, $IDFTSHFT\{\cdot\}$ denotes the IDFT shift operation, and \circ denotes the element-wise matrix multiplication.

A^{l-1} has spatial frequency components in the range of $\left[-\frac{f_s}{2}, \frac{f_s}{2}\right]$ in both f_x and f_y axes where $f_s = 1/dx$ is the sampling frequency in the spatial domain. Note that the gap between two samples in the angular spectrum is $f_s = 1/wNdx$. The propagation transfer function at $z = z_0$ $G(z_0)$ is also created in the computation window with a similar number of samples as A^{l-1} . Since the evanescent waves do not propagate energy along the z -axis, they are filtered out using a mask D . The masked propagation transfer function is given by

$$G(z_0) \circ D = \begin{cases} e^{j2\pi z_0 \sqrt{\frac{1}{\lambda^2} - f_x^2 - f_y^2}} & f_x^2 + f_y^2 \leq \frac{1}{\lambda} \\ 0 & f_x^2 + f_y^2 > \frac{1}{\lambda} \end{cases} \quad (18)$$

According to eq. (10), the AS of the field at $z = z_0$ is obtained by the element-wise multiplication of A^{l-1} and the masked propagation transfer function. Then an inverse DFT (IDFT) shift operation is performed followed by a 2D-IDFT operation to get the padded resulting field. Finally, the padding is removed to retrieve the resulting field U^l .

Method	SSIM
MNIST $[0, \pi]$:	
<i>Learnable Fourier Filter</i>	0.8933
Phase (central) + unit amplitude	0.3132
Phase (central) + learned amplitude	0.3945
HeLa $[0, 2\pi]$:	
<i>Learnable Fourier Filter</i>	0.5919
Phase (central) + unit amplitude	0.3748
Phase (central) + learned amplitude	0.3748

Table S3. Effect of the central region of the learned Fourier filter for reconstruction performance : 35%-64% of the original SSIM score is preserved when the central region is only considered.

C. Further Experiments

C.1. Effect of the Central Region of the Learned Fourier Filter

The goal of this experiment is to analyze the effect of the central region of the learned Fourier filter. In this experiment we obtained the learned filter and modified its weights to consider a combination of only the central region, only the outer region, full filter region of the phase weights (retaining the learned phase weights of the filter), with amplitude weights set to unity and retaining the learned amplitude weights. The considered central region was calculated according to the standard method described in Chapter 3. in [22]. The results of the experiments are summarized in Table S3.

Table S3 depicts how the modified filters for each experiment have been able to capture approximately 35% - 64% of the original SSIM by only considering the learned phase weights in the central region with unit amplitude in the entire filter region. It shows the importance of the central region of the learned filters similar to the theoretical implementation of the GPC filter. The slight improvement in SSIM when considering the learned amplitude weights instead of the unit amplitude for the Phase MNIST scenario signifies the importance of the learned amplitude weights (introduced attenuation) in addition to the phase weights in the central region. The importance in attenuating the incoming power appropriately for the reconstruction is demonstrated here. The conducted experiments highlights the similarities in the characteristics of the regions of our learned filters compared to the theoretical implementations of the GPC filter. Overall, our learned filters show *superior performance* by adjusting the amplitude along with the phase of the transmission coefficients in both regions to reconstruct the background and foreground appropriately.

C.2. Towards Generalized Learnable Phase Retrieval

To analyze the ability of our framework to learn a generalized filter, we train the model on 3 different noise datasets namely: 1. Wide Noise, 2. Sparse Noise, 3. Dense Noise datasets that have different noise levels (see section 5.1).

We considered training the proposed model on the noise dataset in two ways: 1. Train to reconstruct the input phase at its output intensity, 2. Train to reconstruct the input phase at its output amplitude. The resultant models are evaluated on phase to intensity conversion task with MNIST and HeLa $[0, \pi]$ (Table S4).

The model trained on the wide noise dataset for phase to amplitude conversion (A) shows similar performance on both datasets, while the same experiment but trained for phase to intensity (B) shows worse performance on both datasets. This indicates that the model trained on phase to amplitude reconstruction with the wide noise dataset surprisingly has better generalizability on phase to intensity reconstruction task on both MNIST and HeLa datasets.

We conduct similar experiments with the sparse and dense noise datasets as well. We observe that the models trained with sparse noise dataset perform (C, D) well with the MNIST dataset while the models trained with dense noise dataset (E, F) perform well with the HeLa dataset. This shows that MNIST, HeLa datasets have similar sparsity-related characteristics compared to sparse, dense noise datasets respectively. This further shows that our model is generalizable among the datasets which have similar sparsity properties as the training dataset.

Dataset	Performance (SSIM \uparrow)	
	MNIST	HeLa $[0, \pi]$
A) Wide noise [*]	0.3898	0.3728
B) Wide noise [†]	0.2536	0.3585
C) Sparse noise [*]	0.5743	0.0698
D) Sparse noise [†]	0.7774	0.1184
E) Dense noise [*]	0.1731	0.3943
F) Dense noise [†]	-0.3694	0.1432

^{*} Noise dataset trained for phase-to-amplitude reconstruction

[†] Noise dataset trained for phase-to-intensity reconstruction

Table S4. Performance evaluation of the learnable Fourier filter on MNIST and HeLa datasets after training on noise datasets.